

## ARTICLE

# Controlling the Co–S Coordination Environment in Co-Doped WS<sub>2</sub> Nanosheets for Electrochemical Oxygen Reduction

Wei Hong,<sup>†a</sup> Erika Meza<sup>†a</sup> and Christina W. Li<sup>\*a</sup>

Received 00th January 20xx,  
Accepted 00th January 20xx

DOI: 10.1039/x0xx00000x

Cobalt sulfide nanomaterials are among the most active and stable catalysts for the electrocatalytic oxygen reduction reaction in pH 7 electrolyte. However, due to the complexity and dynamism of the catalytic surfaces in cobalt sulfide bulk materials, it is challenging to identify and tune the active site structure in order to achieve lower overpotential oxygen reduction reactivity. In this work, we synthesize isolated Co sites supported on colloidal WS<sub>2</sub> nanosheets and develop a synthetic strategy to rationally control the first-shell coordination environment surrounding the adsorbed Co active sites. By studying Co-WS<sub>2</sub> materials with a range of Co–S coordination numbers, we are able to identify the optimal active site for pH 7 oxygen reduction catalysis, which comprises cobalt atoms bound to the WS<sub>2</sub> support with Co–S coordination number of 3–4. The optimized Co-WS<sub>2</sub> material exhibits oxygen reduction onset potential of 0.798 V vs. RHE, which is comparable to the most active bulk phases of cobalt sulfide in neutral electrolyte conditions.

## Introduction

Recent interest in coupling fuel cells and electrolyzers to biological systems has led to an effort to develop electrocatalysts that operate efficiently under biologically-compatible conditions: pH 7 aqueous buffer and ambient pressure and temperature.<sup>1–9</sup> The oxygen reduction reaction (ORR) in neutral media presents catalytic challenges that are distinct from those present in acidic and alkaline electrolytes. The state-of-the-art catalysts in acidic and alkaline media, supported noble metal nanoparticles and metal oxide nanostructures, are susceptible to deactivation in neutral electrolyte due to surface poisoning and catalyst dissolution, respectively.<sup>10–12</sup>

First-row transition metal sulfides have emerged as alternatives to Pt-based catalysts in ORR under a wide range of pH conditions due to their high activity, stability, and low cost.<sup>9, 13–18</sup> Literature studies have focused primarily on tuning the structure of nickel and cobalt sulfides to understand the role that metal sulfide phase and composition play in dictating ORR reactivity.<sup>19–25</sup> The Co<sub>9</sub>S<sub>8</sub> phase, in particular, has been identified as uniquely active amongst the first-row transition metal sulfides for alkaline and neutral ORR and has been studied in a wide range of composite nanostructures.<sup>26–33</sup> Computational studies have postulated that the M–S coordination environment at the catalytic surface influences oxygen adsorbate binding energies and thus ORR catalytic turnover.<sup>34,</sup>

<sup>35</sup> However, when experimentally altering the crystal structure or composition of a bulk metal sulfide phase, it is challenging to isolate the role that coordination environment plays amidst the multiple geometries and oxidation states that exist within any given phase as well as the dynamic nature of the surface under electrocatalytic conditions.<sup>35, 36</sup>

Supported single atom catalysts (SACs) are intriguing model systems for catalytic surface sites on bulk materials because their active site structure can be studied at the atomic level.<sup>37–39</sup> Previous work on single metal atoms supported on metal oxide and heteroatom-doped carbon materials has shown the importance of local coordination environment and metal-support interaction in influencing catalyst selectivity and reactivity.<sup>40–44</sup> Particular effort has been invested in active site characterization for metal single atoms supported on N-doped carbon.<sup>45–49</sup> Recent work on Co SACs have postulated that the number and chemical nature of nitrogen atoms in the first coordination shell may have an impact on catalytic activity in the alkaline oxygen reduction reaction.<sup>50, 51</sup> While different single atom coordination environments have been observed in these examples, it remains challenging to synthetically control the coordination environment surrounding a single atom catalyst. Single atoms supported on MoS<sub>2</sub> have also been studied extensively, primarily for use as electrocatalysts in the hydrogen evolution reaction (HER).<sup>52</sup> However, doped first-row transition metal single atoms in MoS<sub>2</sub> are not themselves catalytically active sites for HER but rather serve to tune the electronic and catalytic properties of the MoS<sub>2</sub> surface.<sup>53–55</sup> In this work, we put forward a synthetic strategy to generate cobalt single atoms supported on WS<sub>2</sub> nanosheets, in which the Co–S coordination environment can be explicitly tuned through controlled introduction of excess sulfur. These Co-WS<sub>2</sub> nanosheets provide the basis for a systematic study on how the local coordination environment of surface cobalt sulfide active

<sup>a</sup> Department of Chemistry, Purdue University, West Lafayette, IN 47907, USA

<sup>†</sup> These authors contributed equally to this work.

Electronic Supplementary Information (ESI) available: Materials, synthetic methods, physical characterization methods, electrochemical methods, and additional tables and figures. See DOI: 10.1039/x0xx00000x

sites influence oxygen reduction reactivity in neutral electrolyte.

## Experimental Methods

**Synthesis of Colloidal Co-Doped WS<sub>2</sub> Nanosheets.** Colloidal 1T-WS<sub>2</sub> nanosheets capped with oleylamine were synthesized based on a previously reported method.<sup>56, 57</sup> To the dried WS<sub>2</sub> nanosheets (26.2 mg, 0.007 mmol), a 0.1 M solution of *n*-BuLi in hexanes (10 mL) was added under inert atmosphere and stirred for 2 hours. The Li-treated nanosheets (Li-WS<sub>2</sub>) were then rinsed with excess hexanes and redispersed in NMF. To a 1 mL solution of Li-WS<sub>2</sub>, a Co precursor solution (30  $\mu$ L or 100  $\mu$ L of 70 mM CoCl<sub>2</sub> in NMF) was then added and stirred for 24 hours at room temperature under nitrogen. After the Co functionalization step, the nanosheets were precipitated with ethanol (10 mL) and hexanes (20 mL) followed by centrifugation at 8700 rpm for 10 minutes. The supernatant was decanted and the cleaning step was repeated one time.

**K<sub>2</sub>S Impregnation and Annealing Treatment for Co-WS<sub>2</sub>.** The colloidal Co-WS<sub>2</sub> nanosheets were first supported on carbon black by mixing 1 mL of a 7 mM solution of Co-WS<sub>2</sub> nanosheets with 11.6 mg carbon in 4 mL ethanol at room temperature. The supported Co-WS<sub>2</sub> samples were centrifuged at 8700 rpm for 10 min. and resuspended in 2 mL of ethanol:IPA (v/v; 1:3) solution. Next, varying amounts of K<sub>2</sub>S solution (70 mM K<sub>2</sub>S in EtOH) were added, ranging from 0.5 eq. to 10 eq. with respect to Co. The mixture was left stirring in air at room temperature for 24–36 hours until the solvent fully evaporated. The dried powder was then annealed at 300 °C for 2 hours under N<sub>2</sub>. After annealing, the sample was successively rinsed with ethanol, water, and IPA to remove unincorporated K<sub>2</sub>S.

**Scanning/Transmission Electron Microscopy.** Low-resolution TEM images were acquired using an FEI Tecnai T20 TEM equipped with a 200 kV LaB<sub>6</sub> filament. Low-resolution HAADF-STEM imaging and EDS mapping were obtained on an FEI Talos F200X S/TEM with a 200 kV X-FEG field-emission source and a super X-EDS system. High-resolution HAADF-STEM images were collected using a Thermo Scientific Themis Z, a spherical aberration corrected S/TEM with a 300 kV X-FEG field-emission source. Associated EDS spectra were obtained with a quad-silicon FEI Super X drift detector.

In order to obtain atomic-resolution HAADF-STEM images, it is critical to remove all organic ligand and solvent residue from the TEM sample. Colloidal Co-WS<sub>2</sub> samples for HR-STEM were cleaned four additional times with ethanol and hexanes prior to drop casting onto a Au grid coated with an ultrathin carbon film. The Au grid was then submerged in a suspension of carbon black in hexanes, and N<sub>2</sub> gas was bubbled into the solution for 1 min to agitate the suspension.<sup>58</sup> The TEM grid was air-dried and stored under inert atmosphere prior to imaging.

**X-ray Absorption Spectroscopy.** X-ray absorption spectroscopy experiments were carried out at the 10-ID and 10-BM beamlines at the Advanced Photon Source, Argonne National Laboratory. Samples were pressed into a self-supporting pellet, and spectra were obtained in transmission mode at room temperature. The Demeter software package

was used to analyze the collected data.<sup>59</sup> Data was collected at the Co K-edge (7.7089 keV) using metallic Co foil for energy calibration. EXAFS coordination parameters were obtained by a least-squares fit in R-space of the *k*<sup>2</sup>-weighted Fourier transform data from 2.5 to 8.5 Å<sup>-1</sup> for Co-WS<sub>2</sub> samples and 2.5 to 9.0 Å<sup>-1</sup> for control samples. A Co foil reference sample was first fit to its known crystallographic parameters to obtain an amplitude reduction factor (*S*<sub>0</sub><sup>2</sup>) for the Co K-edge. EXAFS fitting of the first coordination shell was carried out between 1.1 and 2.3 Å in R-space. Fittings were done by refining bond distances (*R*), coordination numbers (*CN*) and energy shift (*E*<sub>0</sub>). The Debye-Waller factor ( $\sigma^2$ ) was kept constant for each sample.

**Electrochemical Measurements.** Electrochemical experiments were conducted on a Pine WaveDriver 20 Bipotentiostat. A catalyst ink was obtained by sonicating the catalyst powder in a solution containing 75.6% water, 24% IPA, and 0.4% Nafion (v/v) to obtain a nominal concentration of 7 mM based on Co-WS<sub>2</sub>. The working electrode was prepared by drop casting 10  $\mu$ L of the catalyst ink onto a polished glassy carbon electrode with 5 mm diameter. The catalyst film was dried in air for 25 min at a rotation speed of 700 rpm. The counter electrode was a graphite rod. The electrolyte used for all electrochemical experiments was 1.0 M sodium phosphate buffer solution (pH 7) or 0.1 M KOH (pH 13). Currents are reported with anodic current as positive and cathodic current as negative. Potentials were measured against a Ag/AgCl reference electrode (3 M NaCl) and converted to the RHE reference scale using:

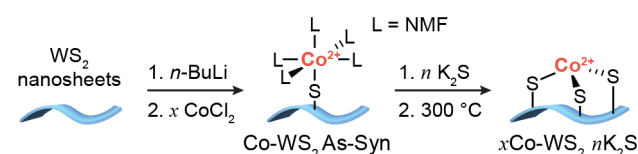
$$E \text{ (vs RHE)} = E \text{ (vs Ag/AgCl)} + 0.210 \text{ V} + 0.0591 \text{ V} \cdot \text{pH}$$

Cyclic voltammetry (CV) scans for Co-WS<sub>2</sub> samples were performed in N<sub>2</sub>-saturated 0.1 M KOH electrolyte with a scan rate of 50 mV/s. Oxygen reduction reaction voltammetry was carried out using a rotating ring-disk electrode in a single-compartment glass cell containing 150 mL of 1.0 M PBS electrolyte. The solution was purged with O<sub>2</sub> for at least 30 min prior to the start of the experiment. For all ORR experiments, a rotation rate of 1600 rpm was utilized. One cathodic linear sweep voltammetry scan was collected at 10 mV/s prior to the reported anodic LSV, obtained by scanning at 1 mV/s from 0.0 V to 0.9 V vs. RHE. The onset potential (*E*<sub>onset</sub>) for ORR is defined to be the potential at which the ORR current density reaches –0.1 mA/cm<sup>2</sup>. All *E*<sub>onset</sub> values are obtained from an average of three sample runs to account for variability in the electrode drop-drying process, and the error bar reflects the standard deviation (**Figure S11–S12**). The Pt ring in the rotating-ring disk electrode was held at 1.26 V vs. RHE during ORR linear sweep voltammetry.

Uncompensated resistances were measured for a set of Co-WS<sub>2</sub> samples, which ranged from 20–36  $\Omega$  in 1.0 M PBS electrolyte. Catalytic measurements are reported without *i*R compensation. To assess the stability of Co-WS<sub>2</sub> catalysts in ORR, galvanostatic electrolysis was performed at –0.25 mA/cm<sup>2</sup> in the standard electrolyte (1 M PBS) as well as with added methanol (1 M MeOH + 1 M PBS). Accelerated CV scanning was performed in a high-purity 1.0 M sodium phosphate electrolyte (pH 7, 99.9%). During the CV stability test, anodic LSV scans at 1

mV/s were obtained in the 1<sup>st</sup>, 5<sup>th</sup>, 20<sup>th</sup>, and 200<sup>th</sup> scan while all intervening CV scans were collected at 200 mV/s (**Figure S16**).

## Results and Discussion



**Scheme 1.** Synthetic strategy for the deposition of Co single atoms onto colloidal WS<sub>2</sub> nanosheets followed by controlled sulfidation and annealing steps.

**Synthesis.** The synthetic strategy to generate Co single atoms with tunable Co–S coordination environment, depicted in Scheme 1, is based on previous work from our group on the synthesis of single atom Ni-doped WS<sub>2</sub> nanosheets.<sup>57</sup> Colloidal WS<sub>2</sub> nanosheets were synthesized via a literature method and activated using *n*-butyllithium (*n*-BuLi) to generate dangling sulfide defects on the basal planes of WS<sub>2</sub> (Li-WS<sub>2</sub>).<sup>56</sup> A dilute solution of CoCl<sub>2</sub> in N-methylformamide (NMF) was then introduced into the colloidal Li-WS<sub>2</sub> nanosheets under an inert atmosphere and permitted to passively adsorb over 24 hours. Any excess CoCl<sub>2</sub> remaining in solution was readily removed through precipitation and centrifugation of the Co-doped WS<sub>2</sub> nanosheets (**Colloidal Co-WS<sub>2</sub>**). Two loadings of Co on WS<sub>2</sub> were synthesized in order to vary the degree of dopant clustering and aggregation – a low loading (0.3 equiv.) to access more isolated Co atoms and a high loading (1.0 equiv.) to generate larger Co aggregates.

In our previous work, we showed that Ni dopants adsorbed relatively weakly and in a monodentate fashion to the WS<sub>2</sub> surface during the colloidal synthesis. In order to tune the Co–S coordination and more strongly anchor the Co dopants to the WS<sub>2</sub> surface, we develop a method herein for controlled sulfidation of the adsorbed Co atoms. The colloidal Co-WS<sub>2</sub> nanosheets are supported on carbon black (***x*Co-WS<sub>2</sub> As-Syn**, where *x* refers to the nominal Co loading) and impregnated with a variable amount of potassium sulfide, ranging from 0.5 to 10 equivalents with respect to the adsorbed Co atoms. The impregnated samples are then annealed at 300 °C under an inert atmosphere and rinsed repeatedly with solvent to remove unreacted sulfides (***x*Co-WS<sub>2</sub> *n*K<sub>2</sub>S**).

**Scanning Transmission Electron Microscopy.** We utilize high-angle annular dark-field scanning transmission electron microscopy (HAADF-STEM) coupled to energy-dispersive X-ray spectroscopy (EDS) to characterize the morphology and elemental distribution of Co and W on the Co-WS<sub>2</sub> nanosheets. Colloidal WS<sub>2</sub> comprises circular nanosheets with ~100 nm diameter and 10–14 layer thickness (**Figure S1a**).<sup>57</sup> After *n*-BuLi activation and Co adsorption, the nanosheet morphology is retained, and Co atoms are evenly distributed across the WS<sub>2</sub> based on the low-resolution HAADF-STEM image and EDS maps (**Figure S1b–f**). Based on EDS, Co loadings on the WS<sub>2</sub> nanosheets follow closely with the amount introduced in solution, ranging from 0.2 up to 1.0 equivalents with respect to

W (**Table S1**). At high Co loading, we anticipate that a significant fraction of Co species may be loosely intercalated or physisorbed within the WS<sub>2</sub> layers rather than coordinatively bound to the surface.

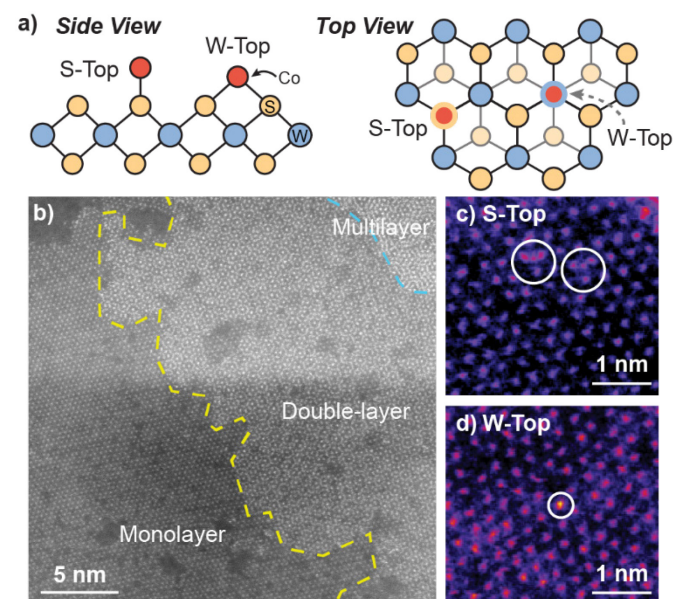


**Figure 1.** (a) Schematic depicting side and top views for S-Top and W-Top binding of Co atoms on WS<sub>2</sub>, (b) high-resolution STEM image of colloidal 0.3Co-WS<sub>2</sub>, (c) HR-STEM region containing S-Top Co sites, and (d) HR-STEM region containing W-Top sites.

High-resolution HAADF-STEM imaging allows us to confirm the presence of Co single atoms in the low loading 0.3Co-WS<sub>2</sub> colloidal nanosheets in two surface adsorption sites (**Figure 1a**). Due to the *n*-BuLi treatment, the underlying WS<sub>2</sub> nanosheets exhibit variable thickness, ranging from monolayer to multilayer, and regions where W vacancies and structural disorder are present (**Figure 1b, S2a**). In the monolayer regions, the ordered hexagonal lattice of W atoms for the WS<sub>2</sub> nanosheet is clearly visible, and deviations to the hexagonal array in terms of both atomic position and contrast provide evidence for the presence of Co single atoms (**Figure 1c–d**). Atoms interstitial to the hexagonal W array, highlighted in Figure 1c and S2b–c, represent Co atoms bound on-top of a S atom or in a S vacancy (S-Top). In addition, analysis of annular-dark field (ADF) Z-contrast shows that Co atoms are also present on-top of W atoms in the hexagonal lattice, highlighted in Figure 1d and S2d–e (W-Top). Interestingly, Co atoms bound in W-Top sites are frequently found adjacent to W vacancies in the lattice, suggesting that dangling sulfide moieties may be responsible for Co coordination in these positions.

In addition to ADF Z-contrast analysis, we also obtained EDS spectra in small regions throughout the high-resolution STEM image to ascertain that Co atoms can be spectroscopically detected on colloidal 0.3Co-WS<sub>2</sub>. While the EDS signal is quite weak when focused on 3 × 3 nm square regions of the monolayer Co-WS<sub>2</sub> nanosheets, we can clearly distinguish peaks associated with the W M, S K $\alpha$ , and Co K $\alpha$  transitions (**Figure S2f–g**). In addition, when the EDS spectra is obtained over a slightly larger region, the atomic ratio of Co:W is ~0.3:1, similar



to the elemental ratios obtained in the lower resolution EDS data.

Prior to sulfur addition, colloidal Co-WS<sub>2</sub> nanosheets are supported on carbon black, which causes the circular nanosheets to fold onto themselves rather than lie flat on the hydrophobic carbon surface (**Figure 2a-b**). Impregnation of 0.5–10 equiv. of K<sub>2</sub>S (with respect to Co) and annealing at 300 °C under N<sub>2</sub> does not alter the overall nanosheet morphology or the average loading of Co relative to W (**Figure 2c-d**, **Figure S3-S4**, **Table S1**). However, we begin to see evidence of Co clustering in the STEM-EDS elemental maps after K<sub>2</sub>S annealing. In 0.3Co-WS<sub>2</sub> samples treated with K<sub>2</sub>S, Co atoms remain colocalized with W and S and evenly distributed across the WS<sub>2</sub> nanosheets in the lower-resolution STEM-EDS maps (**Figure 2c**). Obtaining EDS spectra and quantifying the Co:W ratios at higher resolution reveals spatial variation in the Co distribution on WS<sub>2</sub> (**Figure S5**). In 8 × 8 nm regions across the 0.3Co-WS<sub>2</sub> 3K<sub>2</sub>S sample, we observe Co:W (X:1) ratios ranging from 0.14–0.29, suggesting that Co atoms are beginning to cluster but larger cobalt sulfide nanoparticles have not yet formed on the nanosheets. At the higher loading of Co (1.0Co-WS<sub>2</sub> nK<sub>2</sub>S), cobalt sulfide nanoparticles are observed even in the low-resolution STEM-EDS maps (**Figure 2d**). Aggregates of Co atoms (10–30 nm) that are not co-localized with the underlying W are clearly present.

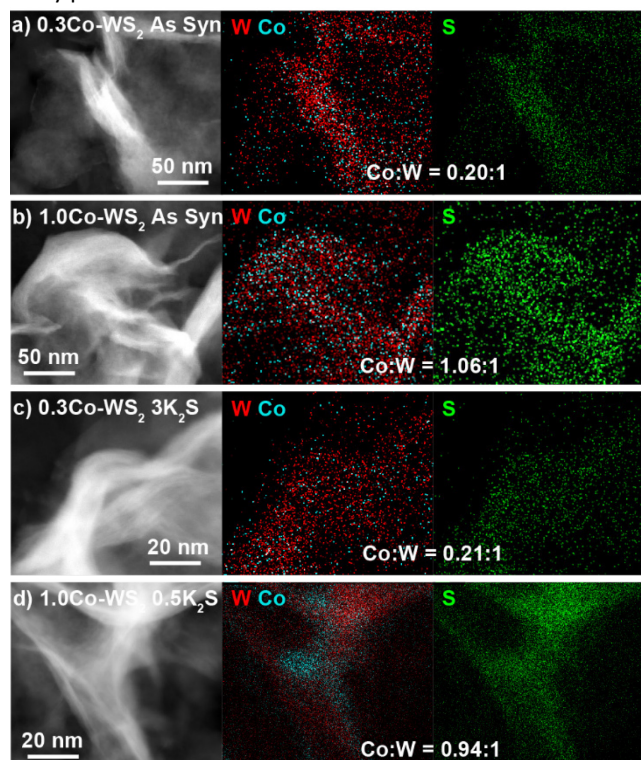


**Figure 2.** STEM-EDS image and elemental maps of W, Co, and S for (a, b) as-synthesized 0.3Co and 1.0Co-WS<sub>2</sub> supported on C as well as (c, d) 0.3Co and 1.0Co-WS<sub>2</sub> after annealing with K<sub>2</sub>S.

Powder X-ray diffraction (XRD) patterns show the expected WS<sub>2</sub> phase transition from 1T to 2H after thermal annealing and no Co-containing crystalline phases (**Figure S6, S7**). In the 1.0Co-

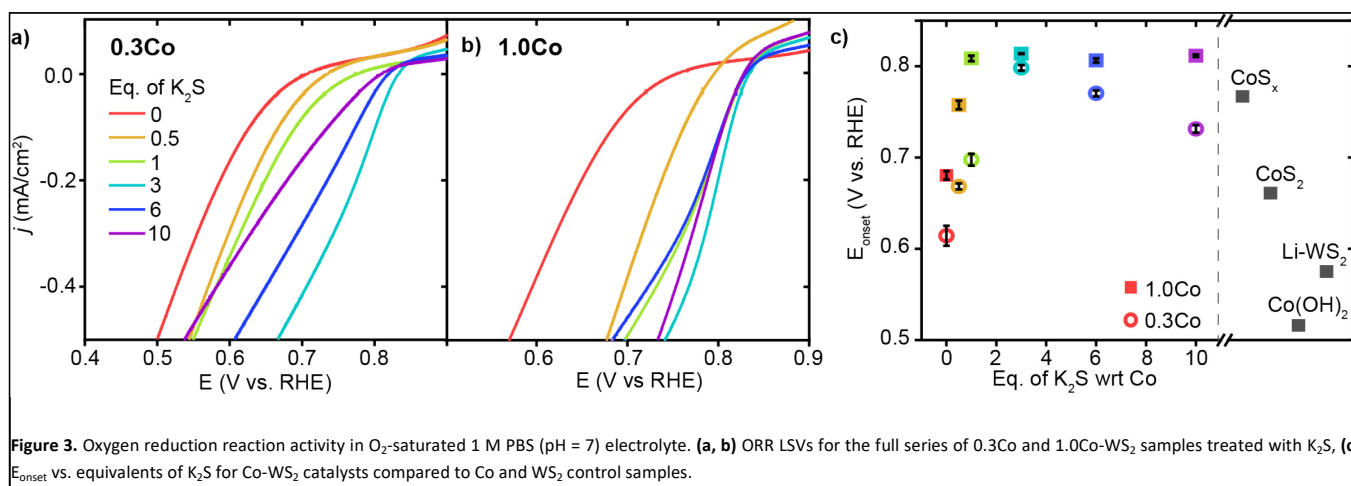
WS<sub>2</sub> nK<sub>2</sub>S samples, the large CoO<sub>x</sub> or CoS<sub>x</sub> aggregates observed in the STEM-EDS maps must therefore be amorphous or comprise many small nanocrystalline domains.

**Oxygen Reduction Reaction.** We began by evaluating the oxygen reduction reactivity of the low and high loading Co-WS<sub>2</sub> catalysts as a function of the amount of K<sub>2</sub>S incorporated during thermal treatment. The ORR catalytic activity of all samples was measured using linear scan voltammetry (LSV) on a rotating ring-disk electrode in O<sub>2</sub>-saturated 1 M phosphate buffer solution (PBS, pH = 7). Negligible ring current is detected using any of the Co-WS<sub>2</sub> catalysts, which indicates quantitative selectivity toward the 4 e<sup>−</sup> reduction of O<sub>2</sub> to H<sub>2</sub>O under these conditions (**Figure S13**). In order to compare the reactivity of various Co-WS<sub>2</sub> and bulk control samples to one another, we utilize the ORR onset potential (*E*<sub>onset</sub>), the potential at which the catalyst attains −0.1 mA/cm<sup>2</sup> of ORR current density, as the primary catalytic metric due to differences in sample mass-transport properties at higher current densities (**Figure S8-S9**).

The annealed Li-WS<sub>2</sub> nanosheets alone show poor ORR activity with *E*<sub>onset</sub> of 0.575 V vs. RHE (**Figure S8**). The addition of Co to the WS<sub>2</sub> sample at low loading (0.3Co-WS<sub>2</sub>) in the absence of K<sub>2</sub>S (0 K<sub>2</sub>S) induces a modest increase in ORR onset potential to 0.614 V vs RHE (**Figure 3a, c**). Introduction of varying equivalents of K<sub>2</sub>S to the 0.3Co-WS<sub>2</sub> sample has a dramatic effect on ORR catalysis. Upon mild sulfidation at 0.5 equiv. K<sub>2</sub>S, the onset potential for ORR immediately increases by 54 mV to 0.668 V vs. RHE. From 0.5 to 3.0 equiv. of K<sub>2</sub>S relative to Co, a steady increase in ORR onset potential is observed with the highest *E*<sub>onset</sub> of 0.798 V vs. RHE occurring at 3.0 equiv. K<sub>2</sub>S. Further increase in K<sub>2</sub>S loading causes a decay in the ORR activity, dropping back down to 0.731 V vs. RHE at 10 equiv. K<sub>2</sub>S. A modest improvement in catalytic activity is also observed when Li-WS<sub>2</sub> alone is annealed in the presence of excess sulfur (**Figure S8**, **Table S2**). However, the onset potential of Li-WS<sub>2</sub> peaks at 0.639 V vs. RHE in the absence of doped Co atoms.

At the higher Co loading (1.0Co-WS<sub>2</sub>), the ORR activity is also sensitive to K<sub>2</sub>S loading but with a somewhat different trend relative to the lower Co loading (**Figure 3b**). In the absence of K<sub>2</sub>S, 1.0Co-WS<sub>2</sub> exhibits an *E*<sub>onset</sub> of 0.680 V vs. RHE. The *E*<sub>onset</sub> rises rapidly with the addition of K<sub>2</sub>S and reaches a peak at 1 equiv. K<sub>2</sub>S, significantly earlier than on the 0.3Co-WS<sub>2</sub> sample (**Figure 3c**). Intriguingly, the *E*<sub>onset</sub> plateaus at this point and stays relatively constant at ~0.81 V vs. RHE even up to 10 equiv. K<sub>2</sub>S. The fast rise and lack of a peak in the onset potential trend is consistent with the presence of aggregated CoS<sub>x</sub> nanoparticles rather than isolated Co atoms or small Co clusters. The lower utilization of Co in the aggregated sample means a smaller amount of K<sub>2</sub>S is required to fully sulfidize the catalytic surface, and excess K<sub>2</sub>S serves only to convert more of the nanoparticle core into sulfided species without further influencing the surface.

Comparing the high and low loading Co-WS<sub>2</sub> at their most active sulfidation point, we find that the ORR onset potentials are quite similar between the two samples despite the very different amounts of Co present (**Figure 3c**). These data further support that the low loading 0.3Co-WS<sub>2</sub> displays excellent



catalytic utilization of Co atoms due to the relatively unaggregated structure of supported Co atoms on WS<sub>2</sub>. For this reason, we believe that the 0.3Co-WS<sub>2</sub> treated with varying equivalents with K<sub>2</sub>S serves as a useful structural model to understand the role of Co–S coordination in dictating ORR reactivity.

To evaluate the catalytic stability of Co-doped WS<sub>2</sub> catalysts, we undertook galvanostatic bulk electrolysis at  $-0.25 \text{ mA/cm}^2$  on the Co-WS<sub>2</sub> 3K<sub>2</sub>S sample and a Pt/C control (Figure S17). While Pt/C is more active, Co-WS<sub>2</sub> is somewhat more stable in 1 M PBS electrolyte. Over 60 min. of electrolysis, the 0.3Co-WS<sub>2</sub> 3K<sub>2</sub>S catalyst decays by 47 mV while Pt/C decays by 90 mV. Notably, when 1 M MeOH is added to the electrolyte, the overpotential required to drive ORR increases by 180 mV on Pt/C due to carbon monoxide poisoning of the Pt surface while remaining essentially unchanged on 0.3Co-WS<sub>2</sub>.

**X-ray Absorption Spectroscopy.** To probe the local coordination environment and electronic state of adsorbed Co atoms in Co-WS<sub>2</sub>, we obtain Co K-edge X-ray absorption spectroscopy (XAS) for Co-WS<sub>2</sub> samples in three states: as-synthesized (As-Syn), K<sub>2</sub>S-treated (K<sub>2</sub>S), and post-catalysis (PBS). These spectra are compared to the precursor molecular complex, Co(NMF)<sub>x</sub>Cl<sub>2</sub>, as well as a control sample of amorphous cobalt sulfide (CoS<sub>x</sub>) with approximate composition of CoS<sub>1.2</sub> (Figure S14, S15).<sup>23,24</sup> Fitting of the Fourier-transformed X-ray absorption fine structure (EXAFS) data was carried out on a subset of samples that showed sufficient Co K-edge absorption, and coordination numbers (CN) and bond distances (*R*) for both Co–O and Co–S scattering were obtained. Full fitting parameters and overlays of fitted and experimental data are provided in Table S4 and Figure S20–22.

The X-ray absorption near edge spectroscopy (XANES) data for the precursor Co(NMF)<sub>x</sub>Cl<sub>2</sub> complex exhibits Co K-edge energy of 7721 eV and high white line intensity, consistent with a Co<sup>2+</sup> ion primarily coordinated to oxygen atoms, as anticipated for a CoCl<sub>2</sub> precursor dissolved in the coordinating solvent NMF (Figure 4a).<sup>60</sup> Likewise, the EXAFS spectrum shows a scattering peak at a short radial distance due to pure Co–O coordination. Fitting of the EXAFS data shows a Co–O bond length of 2.08 Å with CN ~6, consistent with an octahedral molecular complex

(Table 1). On the opposite end of the spectrum, amorphous CoS<sub>x</sub> exhibits a completely suppressed XANES white line and a significantly lower Co K-edge energy of 7714 eV with a strong pre-edge feature at 7710 eV, indicative of mixed tetrahedral and octahedral coordination (Figure 4f).<sup>61</sup> Compared to Co–O coordination, Co–S coordination generates a scattering pathway at higher radial distance due to the longer average bond length, which ranges from 2.18 to 2.45 in known bulk phases of cobalt sulfide (Table S5, Figure S25). The XANES and EXAFS of these two control samples serve as bookends for the Co-WS<sub>2</sub> samples treated with varying amounts of sulfur because we expect the first-shell coordination environment to transform from oxygen-rich to sulfur-rich with increasing K<sub>2</sub>S loading.

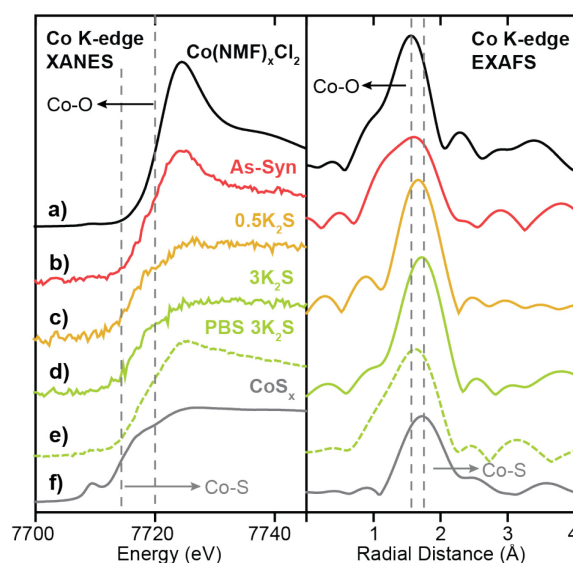


**Figure 4.** Co K-edge XANES and EXAFS spectra for (a) Co(NMF)<sub>x</sub>Cl<sub>2</sub>, (b) As-synthesized 0.3Co-WS<sub>2</sub>, (c) 0.3Co-WS<sub>2</sub> annealed with 0.5 equiv. of K<sub>2</sub>S, (d) 0.3Co-WS<sub>2</sub> annealed with 3.0 equiv. of K<sub>2</sub>S, and (e) amorphous CoS<sub>x</sub>. Dotted lines indicate the edge energies or scattering peaks for Co–O and Co–S coordination.

We begin our XAS analysis with the low loading 0.3Co-WS<sub>2</sub> *n*K<sub>2</sub>S series of samples because their structural homogeneity and lack of aggregation lend themselves to clear structure-activity correlations. In the as-synthesized 0.3Co-WS<sub>2</sub> sample, we observe small perturbations to the adsorbed Co

coordination environment relative to the free  $\text{Co}(\text{NMF})_x\text{Cl}_2$  complex. A drop in white line intensity in the XANES and a small shift to longer radial distance for the first Co–X (X = O or S) scattering pathway relative to the free complex are both indicative of an increase in the number of sulfur atoms relative to oxygen atoms in the first coordination sphere (**Figure 4b**). However, the persistence of the white line peak indicates that Co atoms remain primarily oxygen-bound in this form when passively-adsorbed to the Li-WS<sub>2</sub> nanosheet in the solution phase. These data are consistent with the observation of Co atoms bound in S-Top sites and W-Top sites adjacent to vacancies in the high-resolution STEM images. We postulate that the complex likely binds in a mono- or bidentate fashion to dangling sulfur sites on the lithiated WS<sub>2</sub> surface, and the remaining coordination sites remain occupied by NMF ligands.

Upon K<sub>2</sub>S impregnation and annealing, the XAS data for 0.3Co-WS<sub>2</sub> shows a significant increase in the Co–S coordination to the WS<sub>2</sub> surface. Treatment with 0.5 equiv. or 3 equiv. of K<sub>2</sub>S completely suppresses the sharp white line feature diagnostic of Co<sup>2+</sup>–O binding and shifts the Co K-edge energy downwards by 3 eV, approaching the edge energy of the CoS<sub>x</sub> control sample (**Figure 4c-d**). The EXAFS scattering peak also shifts to longer radial distance, and the sample treated with 3 equiv. K<sub>2</sub>S essentially matches the peak position of CoS<sub>x</sub>. Fitting of the EXAFS data indicates that the Co–S CN of 0.3Co-WS<sub>2</sub> increases steadily from 2.5 at 0.5 equiv. K<sub>2</sub>S up to 3.9 at 3 equiv. K<sub>2</sub>S while the Co–O CN drops correspondingly (**Table 1**). In all of these samples, no significant scattering density is observed beyond 3.0 Å, indicating that Co atoms remain relatively isolated on the WS<sub>2</sub> surface even after thermal annealing. No metallic Co–Co scattering or second coordination sphere Co–X–Co (X = O or S) scattering features are observed based on comparisons to Co foil and a variety of known CoO<sub>x</sub> and CoS<sub>x</sub> crystalline phases (**Figure S20, S25, Table S4, S5**). Together, these data show that Co atomic coordination to the WS<sub>2</sub> surface can be readily controlled in the 0.3Co-WS<sub>2</sub> system simply by varying the amount of impregnated K<sub>2</sub>S.

Lastly, we characterized the 0.3Co-WS<sub>2</sub> samples after 1 hour immersion in phosphate buffer solution, catalytically equivalent to the post-catalysis material after 5–20 CV scans, to understand how the adsorbed Co sites evolve in aqueous electrolyte (**Figure S26, Table S6**). XANES data on 0.3Co-WS<sub>2</sub> 3K<sub>2</sub>S immersed in PBS shows a similar Co K-edge energy but a slight increase in white line intensity relative to the pre-catalysis material (**Figure 4e**). The EXAFS spectrum also shows a small shift in the first-shell scattering peak to lower radial distance. These data indicate that the Co–S bonds that anchor the dopants to the WS<sub>2</sub> surface hydrolyze slightly in the presence of aqueous electrolyte, likely causing the decay in catalytic activity observed in the stability tests (**Figure S16-S17**). However, Co surface sites remain relatively unaggregated on the WS<sub>2</sub> surface after the electrolyte treatment, as evidenced by the continued absence of a second coordination sphere Co–S–Co scattering feature between 3–4 Å (**Figure 4e, Figure S24c**). STEM-EDS mapping and elemental analysis after electrolyte treatment show that Co loading and spatial distribution remain unchanged relative to the pre-catalysis samples (**Figure 5a, Figure S27**). Notably, Co atoms are

fully retained in the 0.3Co-WS<sub>2</sub> *n*K<sub>2</sub>S samples after immersion in aqueous electrolyte, suggesting that all Co atoms are coordinatively attached to the WS<sub>2</sub> surface (**Table S7**).

**Table 1.** Co K-edge EXAFS fitting parameters for  $\text{Co}(\text{NMF})_x$  complex and Co-WS<sub>2</sub> samples at varying synthetic stages including as-synthesized, K<sub>2</sub>S-treated, and PBS-treated.

| Sample   | Pair | CN        | R (Å)        | E <sub>0</sub> (eV) |
|--|------|-----------|--------------|---------------------|
| $\text{Co}(\text{NMF})_x\text{Cl}_2$             | Co–O | 6.0 ± 0.5 | 2.08 ± 0.007 | –2.3 ± 0.9          |
| 0.3Co-WS <sub>2</sub><br>0.5 K <sub>2</sub> S    | Co–O | 3.8 ± 0.2 | 2.10 ± 0.004 | 7.4 ± 0.3           |
|  | Co–S | 2.5 ± 0.1 | 2.25 ± 0.004 |                     |
| 0.3Co-WS <sub>2</sub><br>3 K <sub>2</sub> S      | Co–O | 1.7 ± 0.4 | 2.10 ± 0.022 | 3.3 ± 0.6           |
|  | Co–S | 3.9 ± 0.3 | 2.25 ± 0.006 |                     |
| 1.0Co-WS <sub>2</sub><br>As-Syn                  | Co–O | 4.3 ± 0.4 | 2.08 ± 0.009 | 0.30 ± 0.9          |
| 1.0Co-WS <sub>2</sub><br>0 K <sub>2</sub> S      | Co–O | 4.3 ± 0.3 | 2.08 ± 0.007 | –0.29 ± 0.8         |
| 1.0Co-WS <sub>2</sub><br>1 K <sub>2</sub> S      | Co–O | 5.5 ± 0.4 | 2.10 ± 0.006 | –0.52 ± 0.7         |
| 1.0Co-WS <sub>2</sub><br>3 K <sub>2</sub> S      | Co–O | 4.9 ± 0.2 | 2.10 ± 0.004 | –1.2 ± 0.3          |
|  | Co–S | 0.5 ± 0.1 | 2.25 ± 0.024 |                     |
| 1.0Co-WS <sub>2</sub><br>10 K <sub>2</sub> S     | Co–S | 4.4 ± 0.2 | 2.25 ± 0.005 | –3.1 ± 0.5          |
| 1.0Co-WS <sub>2</sub><br>0 K <sub>2</sub> S PBS  | Co–O | 4.1 ± 0.1 | 2.04 ± 0.003 | –1.0 ± 0.4          |
| 1.0Co-WS <sub>2</sub><br>1 K <sub>2</sub> S PBS  | Co–O | 5.0 ± 0.3 | 2.10 ± 0.006 | –2.1 ± 0.6          |
|  | Co–S | 0.8 ± 0.2 | 2.25 ± 0.025 |                     |
| 1.0Co-WS <sub>2</sub><br>3 K <sub>2</sub> S PBS  | Co–S | 4.5 ± 0.2 | 2.25 ± 0.005 | –4.8 ± 0.5          |
| 1.0Co-WS <sub>2</sub><br>10 K <sub>2</sub> S PBS | Co–S | 4.6 ± 0.4 | 2.25 ± 0.007 | –2.8 ± 0.9          |

We can now correlate XAS structural characterization on the 0.3Co-WS<sub>2</sub> samples to their initial ORR activity because, unlike in bulk or nanoparticle cobalt sulfide materials, the majority of Co atoms are available on the surface for catalysis. We find that 0.3Co-WS<sub>2</sub> treated with 3 equiv. K<sub>2</sub>S, exhibiting three- to four-fold coordination of Co to sulfur atoms on the WS<sub>2</sub> surface, provides an optimal electronic and geometric environment for pH 7 ORR catalysis. We hypothesize that the activation of adsorbed Co atoms with K<sub>2</sub>S up to 3 equiv. stems from the necessity for a more electron-rich metal center, enabled by Co–S coordination, in order to turn over adsorbed OH intermediates in the catalytic cycle.<sup>35, 62</sup> Further increasing K<sub>2</sub>S, however, likely causes over-coordination with sulfur and therefore loss of



available coordination sites for O<sub>2</sub> binding and activation (**Figure S29**). During catalysis, extended exposure to aqueous electrolyte induces partial hydrolysis of Co–S bonds, leading to a slight decay in ORR activity.

As a comparison to our Co-WS<sub>2</sub> materials, we also obtained ORR catalytic data on three Co-containing phases with very different bulk composition and local Co coordination environment: Co(OH)<sub>2</sub>, amorphous CoS<sub>x</sub> (~CoS<sub>1.2</sub>), and CoS<sub>2</sub> (**Figure S14, S15**). The Co(OH)<sub>2</sub> nanosheets with pure Co–O coordination show the poorest ORR onset potential of 0.514 V vs. RHE (**Figure 3c, Table S3**). Even the 0.3Co-WS<sub>2</sub> sample treated with 0 equiv. K<sub>2</sub>S is substantially more active due to the interaction with and contribution of the underlying WS<sub>2</sub> nanosheets. The amorphous CoS<sub>x</sub> sample with an intermediate S:Co ratio of ~1:1 shows the highest E<sub>onset</sub> among the bulk phases at 0.767 V vs. RHE, nearly matching the onset potential of the optimal 0.3Co-WS<sub>2</sub> 3K<sub>2</sub>S catalyst. The most sulfur-rich sample, comprising CoS<sub>2</sub> nanoparticles, exhibits lower ORR activity with an onset potential of 0.660 V vs. RHE, which mirrors the drop in activity of 0.3Co-WS<sub>2</sub> 10K<sub>2</sub>S when it becomes over-saturated with sulfur. The similar trends in onset potential as a function of cobalt sulfidation between 0.3Co-WS<sub>2</sub> and bulk Co-containing phases provides an initial indication that the local coordination environment identified for Co atoms supported on WS<sub>2</sub> may also apply to active sites formed *in-situ* on the surface of bulk cobalt sulfide species during ORR catalysis.

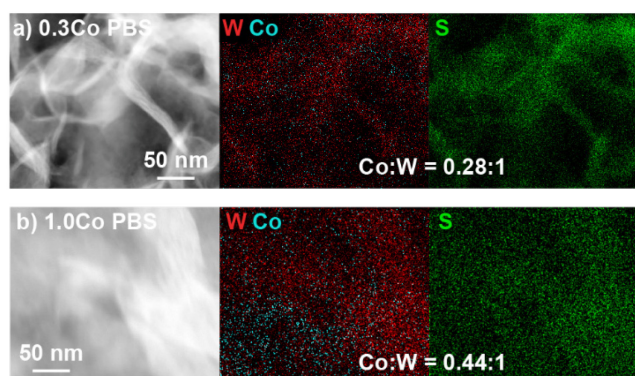


**Figure 5.** STEM-EDS image and elemental maps of W, Co, and S for (a) 0.3Co-WS<sub>2</sub> 3K<sub>2</sub>S and (b) 1.0Co-WS<sub>2</sub> 3K<sub>2</sub>S after treatment with PBS electrolyte.

Because XAS spectra represent an average over all Co species in the sample, the high loading 1.0Co-WS<sub>2</sub> sample, comprising large Co aggregates and heterogeneous speciation, is much more difficult to directly correlate to catalytic reactivity. Nonetheless, the XAS data at each stage of the synthetic and catalytic process provide useful information about the speciation and evolution of adsorbed Co species at high loading.

In the as-synthesized 1.0Co-WS<sub>2</sub>, both the XANES and EXAFS at the Co K-edge closely resemble the spectra for the free Co(NMF)<sub>2</sub>Cl<sub>2</sub> complex, suggesting that a significant fraction of Co complexes at this high loading are intercalated or weakly physisorbed due to the ionic interaction between the negatively charged WS<sub>2</sub> sheets and cationic Co complexes (**Figure 6a**). After K<sub>2</sub>S addition and thermal annealing in the presence of 1 and 3 equiv. K<sub>2</sub>S, small increases in EXAFS first-shell scattering

intensity are observed but with no significant increase in radial distance (**Figure 6b–c**). Coupled to the persistently high white line intensity in the XANES, these data indicate that the bulk of the Co atoms in 1.0Co-WS<sub>2</sub> remain unsulfidized up to 3 equiv. K<sub>2</sub>S (**Table 1**). At 10 equiv. K<sub>2</sub>S, an abrupt increase in first-shell scattering distance and drop in white line intensity reveals that the majority of Co atoms have been converted to cobalt sulfide species (**Figure 6d**). The relatively high equivalents of K<sub>2</sub>S required to sulfidize the Co species in the 1.0Co-WS<sub>2</sub> is consistent with the presence of aggregated and intercalated Co species, clearly indicating that these average XAS spectra are not representative of catalytically active Co species.

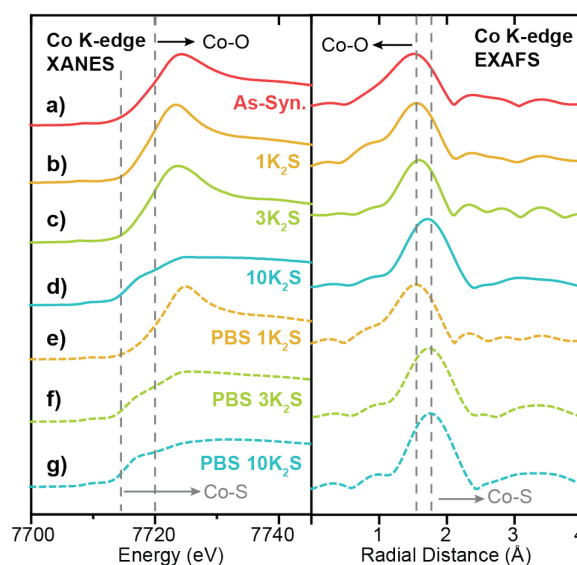


**Figure 6.** Co K-edge XANES and EXAFS spectra for 1.0Co-WS<sub>2</sub> samples at varying stages of synthesis and catalysis. (a) As-synthesized, (b–d) thermally treated with varying equivalents of K<sub>2</sub>S, and (e–g) immersed in 1 M PBS electrolyte. Dotted lines indicate the edge energies or scattering peaks for Co–O and Co–S coordination.

After the PBS immersion, elemental analysis using XRF reveals that significant amounts of Co are leached out of the 1.0Co-WS<sub>2</sub> nanosheets, which is in stark contrast to the full Co retention observed in the 0.3Co-WS<sub>2</sub> samples (**Table S7**). The Co spatial distribution also becomes more non-uniform and aggregated based on STEM-EDS elemental maps after PBS treatment (**Figure 5b, S28, Table S8**). The quantity of leached Co is greatest at low K<sub>2</sub>S loadings, likely because the loosely intercalated Co(NMF)<sub>x</sub> molecular complexes observed in the as-synthesized sample are not yet converted to insoluble CoS<sub>x</sub> aggregates and can be readily removed in strongly ionic solutions. As a result, the post-PBS XAS spectra are likely more representative of the Co species present during catalysis for the high loading 1.0Co-WS<sub>2</sub> sample (**Figure 6e–g**). The difference in XAS spectra between the pre- and post-electrolyte treatment is clearest in the 1.0Co-WS<sub>2</sub> sample at intermediate K<sub>2</sub>S loading (3 K<sub>2</sub>S). While the spectrum prior to PBS immersion appears minimally sulfidized, the spectrum after PBS immersion shows the longer radial distance and suppressed white line intensity characteristic of a cobalt sulfide species (**Figure 6c, f**). This sample clearly demonstrates that unreacted Co complexes after K<sub>2</sub>S annealing are dissolved out during the immersion in

electrolyte solution, leaving behind only the sulfided Co nanoparticles. Analysing the full series of post-PBS samples, we observe an increase in Co–S CN and decrease in Co–O CN as the K<sub>2</sub>S loading is increased (**Table 1**). Full sulfidation is observed by 3 equiv. K<sub>2</sub>S, which exhibits Co–S CN of 4.5 and no contribution from Co–O. Unlike in the 0.3Co-WS<sub>2</sub> samples, however, it is impossible to correlate these average Co–S coordination numbers directly to ORR catalysis because of the presence of large CoS<sub>x</sub> aggregates and the fact that the majority of Co atoms are not available at the surface for catalysis. As anticipated, all 1.0Co-WS<sub>2</sub> samples after PBS treatment display a second coordination sphere Co–X–Co (X = O or S) scattering feature, which corroborates the presence of large aggregates and nanoparticles observed in the STEM-EDS images (**Figure S24**).

## Conclusion

In conclusion, we find that relatively isolated Co atoms supported on WS<sub>2</sub> show high activity for the pH 7 ORR reaction when partially coordinated to sulfur ligands. Both undercoordination and overcoordination to sulfur prove detrimental to catalysis. The optimal Co active site comprises approximate 3–4-fold coordination to sulfur atoms on the surface of WS<sub>2</sub> and two labile coordination sites occupied by oxygen-based solvent ligands. These dilute Co-WS<sub>2</sub> catalysts show similar catalytic activity to the most active bulk phases of cobalt sulfide with an onset potential for ORR of 0.798 V vs. RHE in pH 7 phosphate buffer electrolyte. Unlike bulk CoS<sub>x</sub> systems, however, the majority of Co atoms in dilute Co-WS<sub>2</sub> are available for catalysis, and the Co coordination environment obtained by XAS is representative of catalytically active sites. As a result, we postulate that the optimal coordination environment ascertained herein may be representative of the dynamic active sites present *in situ* on the surfaces of bulk cobalt sulfide catalysts. The activity of dilute Co-WS<sub>2</sub> clearly illustrates that the electronic and geometric environment created by Co-S bonds in the first coordination sphere provides a key descriptor for ORR catalysis in cobalt sulfide materials.

## Author Contributions

WH and EM contributed equally to this work.

## Conflicts of interest

There are no conflicts to declare.

## Acknowledgements

This research was supported by Purdue University. EM and WH acknowledge support from the Purdue Research Foundation. We acknowledge Dr. Rosa E. Diaz for assistance in collecting high resolution HAADF-STEM images. We thank Dr. Yujia Ding, Dr. Kamil Kucuk, Dr. Mark Warren, and Dr. Joshua Wright for

their help with XAS experiments. Use of the Advanced Photon Source is supported by the U.S. Department of Energy, Office of Science, Office of Basic Energy Sciences, under Contract DE-AC02-06CH11357. MCRAT operations are supported by the Department of Energy and MRCAT member institutions.

## References

1. C. Santoro, C. Arbizzani, B. Erable and I. Ieropoulos, *J. Power Sources*, 2017, **356**, 225–244.
2. B. E. Logan, B. Hamelers, R. A. Rozendal, U. Schröder, J. Keller, S. Freguia, P. Aelterman, W. Verstraete and K. Rabaey, *Environ. Sci. Technol.*, 2006, **40**, 5181–5192.
3. M. V. Kannan and G. G. Kumar, *Biosens Bioelectron.*, 2016, **77**, 1208–1220.
4. Z. X. Hu, X. X. Zhou, Y. Lu, R. M. Jv, Y. Liu, N. Li and S. W. Chen, *Electrochim. Acta*, 2019, **296**, 214–223.
5. M. Kodali, S. Herrera, S. Kabir, A. Serov, C. Santoro, I. Ieropoulos and P. Atanassov, *Electrochim. Acta*, 2018, **265**, 56–64.
6. L. Z. Liu, G. Zeng, J. X. Chen, L. L. Bi, L. M. Dai and Z. H. Wen, *Nano Energy*, 2018, **49**, 393–402.
7. X. H. Tang and H. Y. Ng, *Electrochim. Acta*, 2017, **247**, 193–199.
8. O. Schaetzle, F. Barriere and U. Schroder, *Energy Environ. Sci.*, 2009, **2**, 96–99.
9. B. Yan, N. M. Concannon, J. D. Milshtein, F. R. Brushett and Y. Surendranath, *Angew. Chem. Int. Ed.*, 2017, **56**, 7496–7499.
10. J. M. Falkowski, N. M. Concannon, B. Yan and Y. Surendranath, *J. Am. Chem. Soc.*, 2015, **137**, 7978–7981.
11. P. W. Cai, J. H. Huang, J. X. Chen and Z. H. Wen, *Angew. Chem. Int. Ed.*, 2017, **56**, 4858–4861.
12. W. W. Zhao, P. Bothra, Z. Y. Lu, Y. B. Li, L. P. Mei, K. Liu, Z. H. Zhao, G. X. Chen, S. Back, S. Siahrostami, A. Kulkarni, J. K. Nørskov, M. Bajdich and Y. Cui, *ACS Appl. Energy Mater.*, 2019, **2**, 8605–8614.
13. H. Behret, H. Binder and G. Sandstedt, *Electrochim. Acta*, 1975, **20**, 111–117.
14. H. Behret, H. Binder, W. Clauberg and G. Sandstedt, *Electrochim. Acta*, 1978, **23**, 1023–1029.
15. Y. J. Feng, A. Gago, L. Timperman and N. Alonso-Vante, *Electrochim. Acta*, 2011, **56**, 1009–1022.
16. M. R. Gao, J. Jiang and S. H. Yu, *Small*, 2012, **8**, 13–27.
17. V. Vij, S. Sultan, A. M. Harzandi, A. Meena, J. N. Tiwari, W. G. Lee, T. Yoon and K. S. Kim, *ACS Catal.*, 2017, **7**, 7196–7225.
18. H. L. Wang, Y. Y. Liang, Y. G. Li and H. J. Dai, *Angew. Chem. Int. Ed.*, 2011, **50**, 10969–10972.
19. L. Zhu, D. Susac, M. Teo, K. C. Wong, P. C. Wong, R. R. Parsons, D. Bizzotto, K. A. R. Mitchell and S. A. Campbell, *J. Catal.*, 2008, **258**, 235–242.
20. D. Susac, L. Zhu, M. Teo, A. Sode, K. C. Wong, P. C. Wong, R. R. Parsons, D. Bizzotto, K. A. R. Mitchell and S. A. Campbell, *J. Phys. Chem. C*, 2007, **111**, 18715–18723.
21. A. Arunchander, S. G. Peera and A. K. Sahu, *ChemElectroChem*, 2017, **4**, 1544–1553.
22. J. M. Falkowski and Y. Surendranath, *ACS Catal.*, 2015, **5**, 3411–3416.



23. Y. F. Cao, Y. Y. Meng, S. C. Huang, S. M. He, X. H. Li, S. F. Tong and M. M. Wu, *ACS Sustain. Chem. Eng.*, 2018, **6**, 15582-15590.
24. P. Ganesan, M. Prabu, J. Sanetuntikul and S. Shanmugam, *ACS Catal.*, 2015, **5**, 3625-3637.
25. B. L. Chen, R. Li, G. P. Ma, X. L. Gou, Y. Q. Zhu and Y. D. Xia, *Nanoscale*, 2015, **7**, 20674-20684.
26. Q. L. Zhu, W. Xia, T. Akita, R. Q. Zou and Q. Xu, *Adv. Mater.*, 2016, **28**, 6391-6398.
27. Z. X. Wu, J. Wang, M. Song, G. M. Zhao, Y. Zhu, G. T. Fu and X. E. Liu, *ACS Appl. Mater. Interfaces*, 2018, **10**, 25415-25421.
28. Y. X. Zhou, H. B. Yao, Y. Wang, H. L. Liu, M. R. Gao, P. K. Shen and S. H. Yu, *Chem-Eur. J.*, 2010, **16**, 12000-12007.
29. Y. P. Tang, F. Jing, Z. X. Xu, F. Zhang, Y. Y. Mai and D. Q. Wu, *ACS Appl. Mater. Interfaces*, 2017, **9**, 12340-12347.
30. S. F. Fu, C. Z. Zhu, J. H. Song, S. Feng, D. Du, M. H. Engelhard, D. D. Xiao, D. S. Li and Y. H. Lin, *ACS Appl. Mater. Interfaces*, 2017, **9**, 36755-36761.
31. Z. Xiao, G. Z. Xiao, M. H. Shi and Y. Zhu, *ACS Appl. Mater. Interfaces*, 2018, **10**, 16436-16448.
32. S. L. Zhang, D. Zhai, T. T. Sun, A. J. Han, Y. L. Zhai, W. C. Cheong, Y. Liu, C. L. Su, D. S. Wang and Y. D. Li, *Appl. Catal., B*, 2019, **254**, 186-193.
33. F. Bai, X. Qu, J. Wang, X. Chen and W. S. Yang, *ACS Appl. Mater. Interfaces*, 2020, **12**, 33740-33750.
34. R. A. Sidik and A. B. Anderson, *J. Phys. Chem. B*, 2006, **110**, 936-941.
35. B. Yan, D. Krishnamurthy, C. H. Hendon, S. Deshpande, Y. Surendranath and V. Viswanathan, *Joule*, 2017, **1**, 600-612.
36. D. Susac, A. Sode, L. Zhu, P. C. Wong, M. Teo, D. Bizzotto, K. A. R. Mitchell, R. R. Parsons and S. A. Campbell, *J. Phys. Chem. B*, 2006, **110**, 10762-10770.
37. X. F. Yang, A. Q. Wang, B. T. Qiao, J. Li, J. Y. Liu and T. Zhang, *Acc. Chem. Res.*, 2013, **46**, 1740-1748.
38. A. Q. Wang, J. Li and T. Zhang, *Nat. Rev. Chem.*, 2018, **2**, 65-81.
39. G. Giannakakis, M. Flytzani-Stephanopoulos and E. C. H. Sykes, *Acc. Chem. Res.*, 2019, **52**, 237-247.
40. Y. Xin, N. N. Zhang, Q. Li, Z. L. Zhang, X. M. Cao, L. R. Zheng, Y. W. Zeng and J. A. Anderson, *ACS Catal.*, 2018, **8**, 1399-1404.
41. G. Q. Gan, X. Y. Li, L. Wang, S. Y. Fan, J. C. Mu, P. L. Wang and G. H. Chen, *ACS Nano*, 2020, **14**, 9929-9937.
42. Y. Xu, M. Y. Chu, F. F. Liu, X. C. Wang, Y. Liu, M. H. Cao, J. Gong, J. Luo, H. P. Lin, Y. Y. Li and Q. Zhang, *Nano Lett.*, 2020, **20**, 6865-6872.
43. J. Q. Zhang, Y. F. Zhao, C. Chen, Y. C. Huang, C. L. Dong, C. J. Chen, R. S. Liu, C. Y. Wang, K. Yan, Y. D. Li and G. X. Wang, *J. Am. Chem. Soc.*, 2019, **141**, 20118-20126.
44. Q. Wang, X. Huang, Z. L. Zhao, M. Y. Wang, B. Xiang, J. Li, Z. X. Feng, H. Xu and M. Gu, *J. Am. Chem. Soc.*, 2020, **142**, 7425-7433.
45. A. Zitolo, V. Goellner, V. Armel, M. T. Sougrati, T. Mineva, L. Stievano, E. Fonda and F. Jaouen, *Nat. Mater.*, 2015, **14**, 937-942.
46. L. L. Zhang, A. Q. Wang, W. T. Wang, Y. Q. Huang, X. Y. Liu, S. Miao, J. Y. Liu and T. Zhang, *ACS Catal.*, 2015, **5**, 6563-6572.
47. M. Y. Hu, S. N. Li, S. S. Zheng, X. H. Liang, J. X. Zheng and F. Pan, *J. Phys. Chem. C*, 2020, **124**, 13168-13176.
48. W. G. Liu, L. L. Zhang, W. S. Yan, X. Y. Liu, X. F. Yang, S. Miao, W. T. Wang, A. Q. Wang and T. Zhang, *Chem. Sci.*, 2016, **7**, 5758-5764.
49. W. G. Liu, L. L. Zhang, X. Liu, X. Y. Liu, X. F. Yang, S. Miao, W. T. Wang, A. Q. Wang and T. Zhang, *J. Am. Chem. Soc.*, 2017, **139**, 10790-10798.
50. A. Zitolo, N. Ranjbar-Sahraie, T. Mineva, J. K. Li, Q. Y. Jia, S. Stamatini, G. F. Harrington, S. M. Lyth, P. Krtil, S. Mukerjee, E. Fonda and F. Jaouen, *Nat. Commun.*, 2017, **8**.
51. P. Q. Yin, T. Yao, Y. Wu, L. R. Zheng, Y. Lin, W. Liu, H. X. Ju, J. F. Zhu, X. Hong, Z. X. Deng, G. Zhou, S. Q. Wei and Y. D. Li, *Angew. Chem. Int. Ed.*, 2016, **55**, 10800-10805.
52. P. Vancso, Z. I. Popov, J. Peto, T. Ollar, G. Dobrik, J. S. Pap, C. Y. Hwang, P. B. Sorokin and L. Tapasztó, *ACS Energy Lett.*, 2019, **4**, 1947-1953.
53. L. Ji, P. F. Yan, C. H. Zhu, C. Y. Ma, W. Z. Wu, C. Wei, Y. L. Shen, S. Q. Chu, J. O. Wang, Y. Du, J. Chen, X. A. Yang and Q. Xu, *Appl. Catal., B*, 2019, **251**, 87-93.
54. K. Qi, X. Q. Cui, L. Gu, S. S. Yu, X. F. Fan, M. C. Luo, S. Xu, N. B. Li, L. R. Zheng, Q. H. Zhang, J. Y. Ma, Y. Gong, F. Lv, K. Wang, H. H. Huang, W. Zhang, S. J. Guo, W. T. Zheng and P. Liu, *Nat. Commun.*, 2019, **10**.
55. Q. Wang, Z. L. Zhao, S. Dong, D. S. He, M. J. Lawrence, S. B. Han, C. Cai, S. H. Xiang, P. Rodriguez, B. Xiang, Z. G. Wang, Y. Y. Liang and M. Gu, *Nano Energy*, 2018, **53**, 458-467.
56. B. Mahler, V. Hoepfner, K. Liao and G. A. Ozin, *J. Am. Chem. Soc.*, 2014, **136**, 14121-14127.
57. E. Meza, R. E. Diaz and C. W. Li, *ACS Nano*, 2020, **14**, 2238-2247.
58. C. Li, A. P. Tardajos, D. Wang, D. Choukroun, K. Van Daele, T. Breugelmans and S. Bals, *Ultramicroscopy*, 2021, **221**.
59. B. Ravel and M. Newville, *J. Synchrotron Radiat.*, 2005, **12**, 537-541.
60. M. Uchikoshi and K. Shinoda, *Struct. Chem.*, 2019, **30**, 945-954.
61. L. van Haandel, G. Smolentsev, J. A. van Bokhoven, E. J. M. Hensen and T. Weber, *ACS Catal.*, 2020, **10**, 10978-10988.
62. J. K. Nørskov, J. Rossmeisl, A. Logadottir, L. Lindqvist, J. R. Kitchin, T. Bligaard and H. Jonsson, *J. Phys. Chem. B*, 2004, **108**, 17886-17892.